PHYSICAL REVIEW LETTERS **128,** 188001 (2022)

Editors' Suggestion

Tuning Stoichiometry to Promote Formation of Binary Colloidal Superlattices

R. Allen LaCour, Timothy C. Moore, and Sharon C. Glotzer*

Department of Chemical Engineering, The University of Michigan, Ann Arbor, Michigan 48109, USA
Biointerfaces Institute, The University of Michigan, Ann Arbor, Michigan 48109, USA

(Received 11 December 2021; revised 27 March 2022; accepted 31 March 2022; published 2 May 2022)

The self-assembly of binary nanoparticle superlattices from colloidal mixtures is a promising method for the fabrication of complex colloidal cocrystal structures. However, binary mixtures often form amorphous or metastable phases instead of the thermodynamically stable phase. Here we show that in binary mixtures of differently sized spherical particles, an excess of the smaller component can promote—and, in some cases, may be necessary for—the self-assembly of a binary cocrystal. Using computer simulations, we identify two mechanisms responsible for this phenomenon. First, excess small particles act like plasticizers and enable systems to reach a greater supersaturation before kinetic arrest occurs. Second, they can disfavor competing structures that may interfere with the growth of the target structure. We find the phase behavior of simulated mixtures of nearly hard spheres closely matches published experimental results. We demonstrate the generality of our findings for mixtures of particles of arbitrary shape by presenting a binary mixture of hard shapes that only self-assembles with an excess of the smaller component.

DOI: 10.1103/PhysRevLett.128.188001

Binary colloidal mixtures are known to self-assemble into a diverse array of binary superlattices, providing a simple way to prepare colloidal cocrystals with novel combinations of properties [1–9]. The structure of the superlattice dictates important material properties, e.g., photonic response [10] and catalytic activity [11]; thus much effort has focused on designing particles that self-assemble particular colloidal crystal structures [12–19]. However, the self-assembly of cocrystal phases appears particularly susceptible to kinetic limitations, as these phases frequently fail to assemble, instead forming glasses [20–23] or metastable phases [24,25].

In this Letter we demonstrate, using computer simulation, that variation of the stoichiometry can enhance the kinetics of cocrystal self-assembly in binary mixtures whose components differ in size. Self-assembly of binary crystals is usually attempted "on stoichiometry," in which the initial fluid phase has the same stoichiometry as the target crystal [22,26–29]. We show that going "off stoichiometry" by adding an excess of the smaller component can dramatically improve self-assembly. We demonstrate that this enhancement can be attributed to two mechanisms, both of which we observe in our simulations. Specifically, we show that an excess of small particles (i) enables the large component to remain mobile at higher supersaturation, facilitating self-assembly of the equilibrium structure and avoiding kinetic arrest; and (ii) can disfavor competing structures that may interfere with the growth of the equilibrium structure.

We first investigate an additive binary inverse power law (IPL) system with a power of 50 and a size ratio (γ) of 0.55. The particles are characterized by purely repulsive interactions, similarly to many experimental colloids [1,2,30,31]. Setting the power n to 50 makes the particles similar in softness (i.e., steepness of repulsion with interparticle distance—less steep is softer) to some experimental microgels [2] but slightly softer than most PMMA beads [32]. We make them slightly soft so as to be able to use standard molecular dynamics (MD) algorithms; from our previous work [33] and the phase diagram computed here, we do not expect their phase behavior to deviate significantly from hard spheres. We used HOOMD-blue [34–36] to conduct, FREUD [37] to analyze, and SIGNAC [38] to organize the MD simulations. Full simulation methodology is provided in section S1 of the Supplemental Material [37–47]. We describe stoichiometry throughout this Letter in two ways: using the number ratio $N_L:N_S$ or the fraction of small particles $x_S = N_S/(N_L + N_S)$. We give distances in terms of the diameter σ of the large particles and energies in terms of the energy scale ϵ of the IPL.

Via free energy calculations [42,44] (S2 of the Supplemental Material), we computed the thermodynamic phase diagram of the binary IPL model at $kT/\epsilon = 1$, as shown in Fig. 1, plotted in terms of reduced pressure $P^* = P\sigma^3/\epsilon$ and x_S. Because of comparable experimental [1] and simulation [8] studies, we considered the following candidate phases: a face-centered cubic crystal of the large particles (FCC$_L$), a face-centered cubic crystal of the small particles (FCC$_S$), an AlB$_2$ cocrystal, a NaZn$_{13}$ cocrystal, and the fluid phase. Their stoichiometries $N_L:N_S$ are 1:0, 0:1, 1:2, and 1:13, respectively. We assume there is no compositional disorder in the solids at equilibrium, so at any stoichiometry besides their own (e.g., $x_S = 2/3$ for AlB$_2$), they must coexist with another phase.

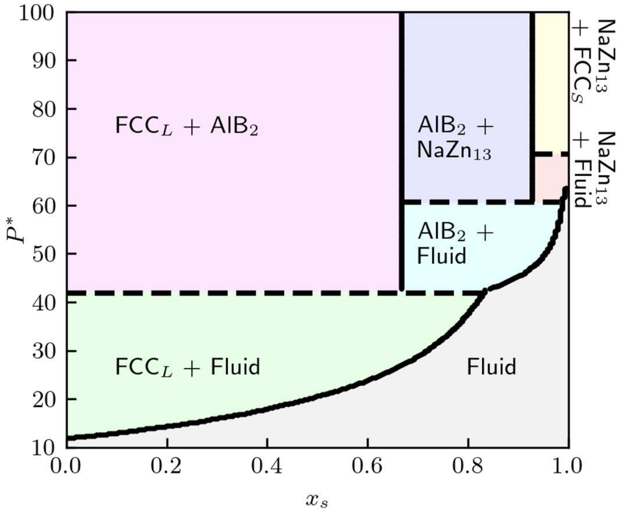

FIG. 1. Thermodynamic phase diagram for the binary inverse power law model (IPL) at $\gamma = 0.55$, $n = 50$, and $kT/\epsilon = 1$. Five phases are present: fluid, FCC$_L$, FCC$_S$, AlB$_2$, and NaZn$_{13}$. Dashed lines indicate three-phase coexistence.

The phase diagram tells us the equilibrium phase(s) for a given set of conditions, but does not tell us whether the phases are kinetically accessible. For self-assembly to occur, the average time for another phase to nucleate and grow must be shorter than the time accessible in experiment (or simulation). Both nucleation and growth rates are strongly influenced by the degree of supersaturation. For a fluid-to-solid transition, increasing the degree of supersaturation has contrasting effects: the free energy barrier for nucleation decreases, favoring assembly, but the particle mobility decreases, disfavoring assembly [48]. If the mobility decreases too much before the free energy barrier becomes surmountable, the particles become kinetically arrested, inhibiting the formation of the equilibrium solid phase.

We first investigate whether AlB$_2$ will homogeneously nucleate from a fluid for a variety of pressures and stoichiometries. The simulations were initialized in a fluidlike state with 27 000 particles and run in the *NPT* ensemble for $4 \times 10^5 \tau$ time steps, where $\tau = \sigma(m/\epsilon)^{1/2}$ and m is particle mass. Because we observed some crystal growth at $N_L\!:\!N_S = 1\!:\!3$ and $P^* = 70$ and wanted to verify that the crystal continued to grow, we continued that simulation for an additional $4 \times 10^5 \tau$ time steps. In Fig. 2(a) we show the evolution in the number of AlB$_2$-like particles up to 200 particles (according to our order parameter; see section S3 of the Supplemental Material) to observe the initial growth of the cocrystal nuclei. We note that, according to our phase diagram, pure AlB$_2$ is expected to form at 1:2, while at 1:3 and 1:5, AlB$_2$ is expected to coexist with a fluid phase or NaZn$_{13}$ (depending upon the pressure). For the set of simulations shown in Fig. 2, we only observe AlB$_2$ coexisting with the fluid.

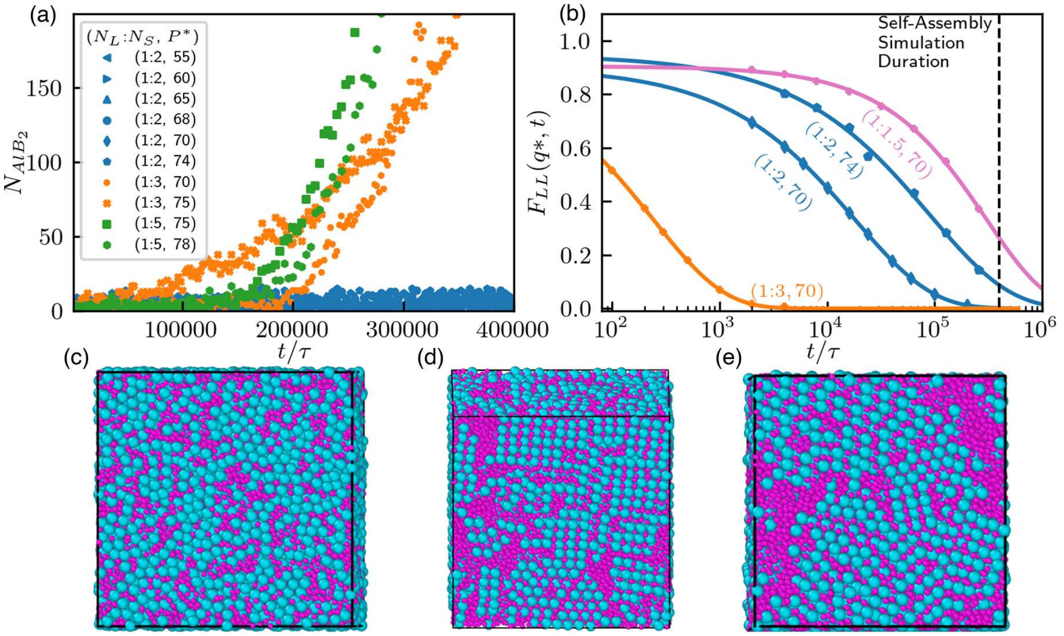

FIG. 2. Self-assembly of AlB$_2$. The plot in (a) shows the evolution of the number of large particles identified as AlB$_2$ for *NPT* simulations at the given pressure and stoichiometry. All simulations at $N_L\!:\!N_S = 1\!:\!2$ (colored blue on the plot) overlap substantially because they never exceed $N_{\mathrm{AlB}2} = 16$. The plot in (b) shows the decay of the intermediate scattering function for certain combinations of stoichiometry and pressure. The lines are fits to the data. The dotted black line indicates the duration of simulations in (a). Snapshots of the results are shown for stoichiometries and pressures of (c) $N_L\!:\!N_S = 1\!:\!2$, $P^* = 70$, (d) $N_L N_S = 1\!:\!3$, $P^* = 70$, and (e) $N_L\!:\!N_S = 1\!:\!5$, $P^* = 75$.

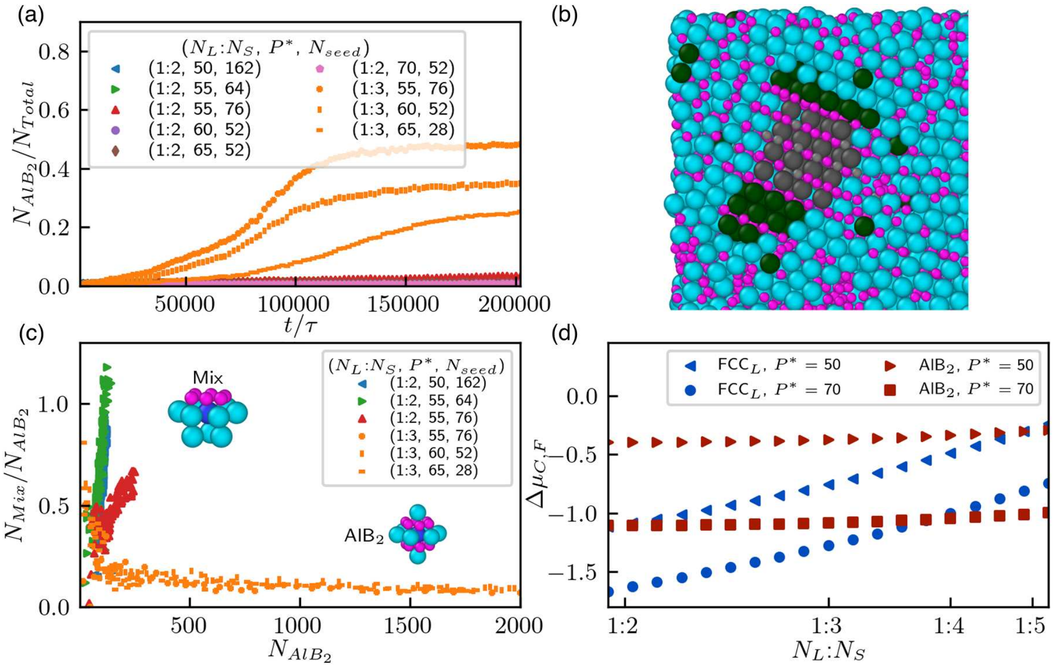

FIG. 3. Crystal growth in seeded simulations. The plot in (a) shows the evolution of the number of large particles identified as AlB$_2$ from seeded simulations for different x_s, $P\sigma^3/\epsilon$, and initial seed size (N_{seed}). The image in (b) is a snapshot of the end of the seeded simulation at $N_L\!:\!N_S = 1\!:\!2$ and $P\sigma^3/\epsilon = 55$. Large and small particles belonging to the initial seed are colored dark grey and light grey, respectively; large particles classified as mixed FCC-AlB$_2$ are colored dark green. The plot in (c) shows the number of particles classified as AlB$_2$ (N_{AlB2}) versus the ratio of the number classified as mixed FCC-AlB$_2$ to N_{AlB2} ($N_{\mathrm{mix}}/N_{\mathrm{AlB2}}$). The insets illustrate the mixed FCC-AlB$_2$ and AlB$_2$ environments. The plot in (d) shows the chemical potential driving force $\Delta\mu_{C,F}$ for the FCC$_L$ and AlB$_2$ as a function of pressure and stoichiometry, where $\Delta\mu_{C,F}$ is defined by Eq. (1). Errors (calculated as described in S2 of the Supplemental Material) are smaller than the size of the points.

Figure 2(a) shows that N_{AlB2} never exceeds 16 for the on-stoichiometry systems at the chosen pressures, indicating that self-assembly never occurs. In contrast, we find that N_{AlB2} increases to 200 and beyond for systems with an excess of small particles. The results are consistent with the system snapshots shown in Figs. 2(c)–2(e), where crystal grains are only apparent at 1:3 and 1:5. We note the presence of small grain sizes, which mirrors the results obtained by Bommineni *et al.* with particle swap moves [49] in binary mixtures of hard spheres. At the highest pressure we simulated for $N_L\!:\!N_S = 1\!:\!2$ ($P^* = 74$), particle mobility is extremely limited, as shown in Fig. 2(b) where we plot the temporal decay of the first peak ($q*$) in the intermediate scattering function calculated for the large particles [$F_{LL}(t)$]. We thus conclude that self-assembly is only possible with an excess of small particles on the timescale of our simulations. We attribute this result in part to particles being more mobile at higher x_s. For example, by fitting the decay of $F_{LL}(t)$ to a stretched exponential [indicated by the lines in Fig. 2(b)], we computed that the structural relaxation time is around 75 times longer at a stoichiometry of 1:2 than at 1:3 ($18\,200\tau$ versus 242τ) at $P^* = 70$, which indicates much slower equilibration at 1:2. We also show the decay of $F_{LL}(t)$ for a system at 1:1.5 and $P^* = 70$, which is an order of magnitude slower than at 1:2. For this reason we did not attempt self-assembly with an excess of large particles. The trend in mobility with stoichiometry stems from the higher freezing and kinetic arrest pressures of the smaller particles relative to the larger component (as can be seen by comparing the P^* at which FCC$_L$ and FCC$_S$ become stable in Fig. 1), which is generally true in size disperse systems of purely repulsive particles.

We next analyze the growth of AlB$_2$ in the presence of crystalline seeds. By construction, these simulations bypass the need to form a critical nucleus and thus may allow self-assembly on shorter timescales than required for homogeneous nucleation. Each simulation was prepared by compressing a fluid around a perfect (constructed) seed of AlB$_2$ and then allowing the fluid and seed to evolve in an *NPT* simulation. The seed crystals were chosen to be small but postcritical, as evidenced by their persistence in the simulations.

Figure 3(a) shows the evolution of the fraction of large particles classified as AlB$_2$-like ($N_{\mathrm{AlB2}}/N_{\mathrm{total}}$). We consistently find more crystal growth off stoichiometry at $N_L\!:\!N_S = 1\!:\!3$, with final values of $N_{\mathrm{AlB_2}}/N_{\mathrm{total}}$ ranging from 0.25 to 0.48, than on stoichiometry, for which $N_{\mathrm{AlB_2}}/N_{\mathrm{total}}$ never rises above 0.035.

Inspection of the growing seeds at $N_L\!:\!N_S = 1\!:\!2$ revealed the accumulation of non-AlB$_2$ layers of particles on the seed [an example at $P^* = 55$ is shown in Fig. 3(b)]. We identified many of these layers to be two (or more) subsequent close-packed planes of large particles. This possibility seemed likely because FCC_L, which consists of close-packed planes, is metastable under the conditions we investigate, and AlB_2 has a close-packed layer of large particles in its structure onto which additional close-packed layers could grow. We call a layer of these particles a "mixed layer" and the associated coordination environment "mixed FCC-AlB_2"; we denote the number of these particles N_{mix}. In Fig. 3(b) we illustrate their presence in dark green for a seed grown at $P^* = 55$ and $N_L:N_S = 1:2$.

We quantify the formation of the mixed layer during the seeded simulations in Fig. 3(c), plotting $N_{\mathrm{mix}}/N_{\mathrm{AlB2}}$ versus N_{AlB2}. For $N_L:N_S = 1:2$ we plot only the results for $P^* \leq 55$ because at higher pressures N_{AlB2} never exceeds 100 (i.e., those seeds grow negligibly over the simulation). Off stoichiometry at $N_L:N_S = 1:3$, the proportion of mixed layers decreases with crystal growth in all cases. In contrast, on stoichiometry at 1:2 the proportion always increases, indicating that mixed layers form more frequently than AlB_2 layers. The formation of the mixed layers instead of the equilibrium AlB_2 phase is similar to previous reports of "self-poisoning" in nucleation, in which the formation of a metastable phase interferes with the growth of the equilibrium phase [24,50].

We identify a thermodynamic reason as to why the mixed layers are more prevalent at $N_L:N_S = 1:2$. Because the mixed layer is essentially the formation of a FCC layer where an AlB_2 layer should have formed, its appearance likely correlates with the thermodynamic stability of the competing FCC_L phase. In Fig. 3(d) we examine the chemical potential driving force for crystallization:

$$\Delta\mu_{C,F} = \hat{G}_C - (1 - x_C)\mu_F^L - x_C \cdot \mu_F^S. \tag{1}$$

The quantity $\hat{G}_C$ is the specific Gibb's free energy of the crystal; x_C is the fraction of small particles in the crystal; and μ_F^L and μ_F^S are the chemical potentials of the large and small species in the fluid, respectively. More negative $\Delta\mu_{C,F}$ values indicate stronger thermodynamic driving forces for crystallization.

Figure 3(d) shows that the $\Delta\mu_{C,F}$ of both crystals decreases with pressure but increases with a greater proportion of small particles. However, we find that $\Delta\mu_{\mathrm{FCC}_L,F}$ is more sensitive to stoichiometry than $\Delta\mu_{\mathrm{AlB}_2,F}$. For example, at $P^* = 70$, changing the stoichiometry from 1:2 to 1:3 increases the $\Delta\mu_{C,F}$ of FCC_L by 0.37 kT while only increasing the $\Delta\mu_{C,F}$ of AlB_2 by 0.02 kT, resulting in a greater preference of the fluid to form AlB_2 relative to FCC_L.

To summarize these results, we find that AlB_2 does not self-assemble or even grow from a seed crystal in an on-stoichiometry fluid. We identified two reasons its formation is inhibited: slow dynamics and interference from a competing phase. Both issues are alleviated by adding an excess of small particles. Adding excess large particles reduces particle mobility and makes FCC_L even more favored relative to AlB_2 and thus will not alleviate the issues.

Our simulations should be most comparable with the experiments of Bartlett *et al.* [1,51] using PMMA particles because our results are for a similar size ratio (0.55 vs 0.58) and they explore how stoichiometry affects assembly. In Table I, we compare the binary crystals we obtain with theirs. Our results at $N_L:N_S$ of 1:2, 1:3, 1:5, are shown in Fig. 2; results for the other stoichiometries are shown in section S4 of the Supplemental Material. We denote any experiment not reported with "⋯".

Overall, we see strong agreement between simulation and the published experimental results. We both obtain an amorphous structure at 1:2, but see AlB_2 with a slight excess of small particles. Around a stoichiometry of 1:9, we both begin to see $NaZn_{13}$ self-assemble, and continue to see it self-assemble at stoichiometries up to 1:30.

To establish whether the self-assembly of other binary crystals may be assisted by an excess of small particles, we also simulated a binary mixture of hard cuboctahedra and octahedra at a volume ratio of 5:1. Despite this mixture being capable of comprising a space-filling CsCl-type structure, previous work found that additional attractive interactions were required for self-assembly [26,52]. In Fig. 4, we present our results for self-assembly conducted at stoichiometries of 1:1 and 1:2 through slow compression in the NVT ensemble. We used 4096 particles due to the higher cost of simulating anisotropic particles [47].

By comparison with the RDFs of perfect CsCl, we identified the result at 1:2 to be CsCl. At 1:1, a single-component structure composed of the large particles self-assembles, while the small particles remain fluidlike. It is thus apparent that, although particle mobility is not limited, the single-component structure (successfully) competes with CsCl when the fluid is on stoichiometry, and an excess of small particles is necessary to observe the thermodynamically preferred binary structure [52]. We

TABLE I. Crystals Observed in Simulation and Experiment.

N_L: N_S	x_S	Simulation structures	Experiment structures[a]
1:2	2/3	Amorphous	Amorphous
1:3	3/4	AlB_2	⋯
1:4	4/5	AlB_2	AlB_2
1:5	5/6	AlB_2	⋯
1:6	6/7	AlB_2	AlB_2
1:9	9/10	$AlB_2/NaZn_{13}$	$NaZn_{13}$
1:13	13/14	$NaZn_{13}$	⋯
1:14	14/15	$NaZn_{13}$	$NaZn_{13}$
1:20	20/21	$NaZn_{13}$	$NaZn_{13}$
1:30	30/31	$NaZn_{13}$	$NaZn_{13}$

[a] Bartlett *et al.* [1].

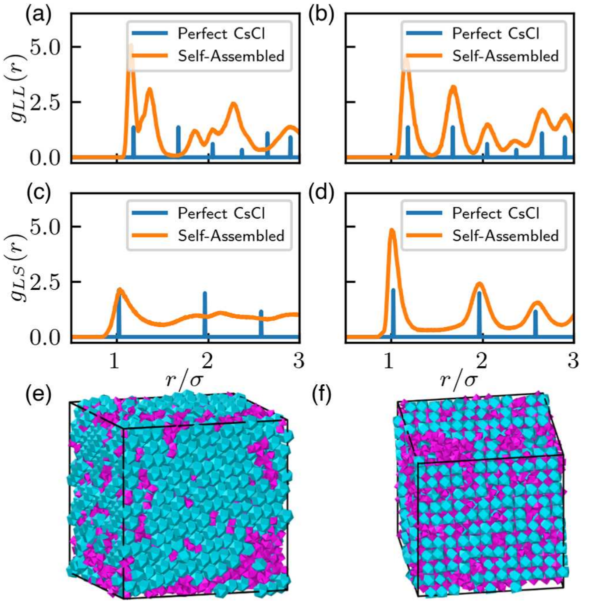

FIG. 4. Self-assembly of hard cuboctahedra and octahedra. The plots show the radial distribution functions (RDFs) averaged over the final few frames of self-assembly at stoichiometries of (a),(c) 1 : 1 and (b),(d) 1 : 2. Also shown are the RDFs for a perfect CsCl structure. We show the RDF for large particles (g_{LL}) and for large and small particles (g_{LS}); the RDF for small particles is dominated by fluidlike small particles. Snapshots of the results are shown for (e) 1 : 1 and (f) 1 : 2.

note a similar trend was recently observed in host-guest structure-forming hard particles [53].

In summary, we demonstrated that the self-assembly of binary nanoparticle superlattices can be promoted by adding an excess of the smaller component to the colloidal fluid mixture. The principles elucidated here are quite general and likely apply to other binary mixtures of size disperse particles, although it is difficult to predict *a priori* which systems require an excess of small particles to cocrystallize. We can say that the enhanced particle mobility should benefit systems which are prone to kinetic arrest, which includes many binary mixtures of purely repulsive particles [22,23,26,28,54]. The enhancement to particle mobility should also increase for smaller size ratios and be limited if the components are similar in size, although depletion will occur for extreme size disparity [55]. Here we observed enhanced self-assembly kinetics in binary mixtures with volume ratios of $0.55^3 \approx 0.166$ and 0.2, and therefore we expect similar enhancement in mixtures with similar volume ratios.

This investigation was supported by the Department of the Navy, Office of Naval Research under ONR Award No. N00014-18-1-2497. This work used resources from the Extreme Science and Engineering Discovery Environment (XSEDE) [56], which is supported by National Science Foundation Grant No. ACI-1548562; XSEDE Award DMR 140129; and also used resources of the Oak Ridge Leadership Computing Facility, which is a DOE Office of Science User Facility supported under Contract No. DE-AC05-00OR22725. Additional computational resources supported by Advanced Research Computing at the University of Michigan.

---

[*] sglotzer@umich.edu

[1] P. Bartlett, R. H. Ottewill, and P. N. Pusey, Superlattice Formation in Binary Mixtures of Hard Sphere Colloids, Phys. Rev. Lett. **68**, 3801 (1992).

[2] N. Schaertl, D. Botin, T. Palberg, and E. Bartsch, Formation of Laves phases in buoyancy matched hard sphere suspensions, Soft Matter **14**, 5130 (2018).

[3] E. V. Shevchenko, D. V. Talapin, N. A. Kotov, S. O'Brien, and C. B. Murray, Structural diversity in binary nanoparticle superlattices, Nature (London) **439**, 55 (2006).

[4] M. A. Boles, M. Engel, and D. V. Talapin, Self-assembly of colloidal nanocrystals: From intricate structures to functional materials, Chem. Rev. **116**, 11220 (2016).

[5] Z. Chen, J. Moore, G. Radtke, H. Sirringhaus, and S. O'Brien, Binary nanoparticle superlattices in the semiconductor-semiconductor system: CdTe and CdSe, J. Am. Chem. Soc. **129**, 15702 (2007).

[6] M. J. Murray and J. V. Sanders, Close-packed structures of spheres of two different sizes II. The packing densities of likely arrangements, Philos. Mag. A **42**, 721 (1980).

[7] S. Hachisu and S. Yoshimura, Optical demonstration of crystalline superstructures in binary mixtures of latex globules, Nature (London) **283**, 188 (1980).

[8] M. D. Eldridge, P. A. Madden, and D. Frenkel, Entropy-driven formation of a superlattice in a hard-sphere binary mixture, Nature (London) **365**, 35 (1993).

[9] M. D. Eldridge, P. A. Madden, P. N. Pusey, and P. Bartlett, Binary hard-sphere mixtures: A comparison between computer simulation and experiment, Mol. Phys. **84**, 395 (1995).

[10] A. P. Hynninen, J. H. Thijssen, E. C. Vermolen, M. Dijkstra, and A. Van Blaaderen, Self-assembly route for photonic crystals with a bandgap in the visible region, Nat. Mater. **6**, 202 (2007).

[11] Y. Kang, X. Ye, J. Chen, L. Qi, R. E. Diaz, V. Doan-Nguyen, G. Xing, C. R. Kagan, J. Li, R. J. Gorte, E. A. Stach, and C. B. Murray, Engineering catalytic contacts and thermal stability: Gold/iron oxide binary nanocrystal superlattices for CO oxidation, J. Am. Chem. Soc. **135**, 1499 (2013).

[12] G. Van Anders, D. Klotsa, A. S. Karas, P. M. Dodd, and S. C. Glotzer, Digital alchemy for materials design: Colloids and beyond, ACS Nano **9**, 9542 (2015).

[13] C. S. Adorf, J. Antonaglia, J. Dshemuchadse, and S. C. Glotzer, Inverse design of simple pair potentials for the self-assembly of complex structures, J. Chem. Phys. **149**, 204102 (2018).

[14] W. D. Piñeros, B. A. Lindquist, R. B. Jadrich, and T. M. Truskett, Inverse design of multicomponent assemblies, J. Chem. Phys. **148**, 104509 (2018).

[15] Z. M. Sherman, M. P. Howard, B. A. Lindquist, R. B. Jadrich, and T. M. Truskett, Inverse methods for design of soft materials, J. Chem. Phys. **152**, 140902 (2020).

[16] P. F. Damasceno, M. Engel, and S. C. Glotzer, Predictive self-assembly of polyhedra into complex structures, Science **337**, 453 (2012).

[17] E. Pretti, H. Zerze, M. Song, Y. Ding, N. A. Mahynski, H. W. Hatch, V. K. Shen, and J. Mittal, Assembly of three-dimensional binary superlattices from multi-flavored particles, Soft Matter **14**, 6303 (2018).

[18] N. A. Mahynski, E. Pretti, V. K. Shen, and J. Mittal, Using symmetry to elucidate the importance of stoichiometry in colloidal crystal assembly, Nat. Commun. **10**, 2028 (2019).

[19] Y. Geng, G. van Anders, P. M. Dodd, J. Dshemuchadse, and S. C. Glotzer, Engineering entropy for the inverse design of colloidal crystals from hard shapes, Sci. Adv. **5**, eaaw0514 (2019).

[20] W. Kob and H. C. Andersen, Scaling Behavior in the β-Relaxation Regime of a Supercooled Lennard-Jones Mixture, Phys. Rev. Lett. **73**, 1376 (1994).

[21] L. Berthierand and G. Biroli, Theoretical perspective on the glass transition and amorphous materials, Rev. Mod. Phys. **83**, 587 (2011).

[22] T. Dasgupta, G. M. Coli, and M. Dijkstra, Tuning the glass transition: Enhanced crystallization of the laves phases in nearly hard spheres, ACS Nano **14**, 3957 (2020).

[23] K. Zhang, W. W. Smith, M. Wang, Y. Liu, J. Schroers, M. D. Shattuck, and C. S. O'Hern, Connection between the packing efficiency of binary hard spheres and the glass-forming ability of bulk metallic glasses, Phys. Rev. E **90**, 032311 (2014).

[24] E. Sanz, C. Valeriani, D. Frenkel, and M. Dijkstra, Evidence for Out-of-Equilibrium Crystal Nucleation in Suspensions of Oppositely Charged Colloids, Phys. Rev. Lett. **99**, 055501 (2007).

[25] R. T. Scarlett, M. T. Ung, J. C. Crocker, and T. Sinno, A mechanistic view of binary colloidal superlattice formation using DNA-directed interactions, Soft Matter **7**, 1912 (2011).

[26] M. R. Khadilkar and F. A. Escobedo, Self-assembly of binary space-tessellating compounds, J. Chem. Phys. **137**, 194907 (2012).

[27] P. K. Bommineni and S. N. Punnathanam, Molecular simulation of homogeneous crystal nucleation of AB_2 solid phase from a binary hard sphere mixture, J. Chem. Phys. **147**, 064504 (2017).

[28] P. K. Bommineni, M. Klement, and M. Engel, Spontaneous Crystallization in Systems of Binary Hard Sphere Colloids, Phys. Rev. Lett. **124**, 218003 (2020).

[29] G. M. Coli and M. Dijkstra, An artificial neural network reveals the nucleation mechanism of a binary colloidal AB13 crystal, ACS Nano **15**, 4335 (2021).

[30] N. Hunt, R. Jardine, and P. Bartlett, Superlattice formation in mixtures of hard-sphere colloids, Phys. Rev. E **62**, 900 (2000).

[31] N. J. Lorenz, J. H. Schope, R. Holger, T. Palberg, P. Wette, I. Klassen, D. Holland-Moritz, D. Herlach, and T. Okubo, Phase behaviour of deionized binary mixtures of charged colloidal spheres, J. Phys. Condens. Matter **21**, 464116 (2009).

[32] C. P. Royall, W. C. K. Poon, and E. R. Weeks, In search of colloidal hard spheres, Soft Matter **9**, 17 (2013).

[33] R. A. LaCour, C. S. Adorf, J. Dshemuchadse, and S. C. Glotzer, Influence of softness on the stability of binary colloidal crystals, ACS Nano **13**, 13829 (2019).

[34] J. A. Anderson, C. D. Lorenz, and A. Travesset, General purpose molecular dynamics simulations fully implemented on graphics processing units, J. Comput. Phys. **227**, 5342 (2008).

[35] J. A. Anderson, J. Glaser, and S. C. Glotzer, HOOMD-blue: A PYTHON package for high-performance molecular dynamics and hard particle Monte Carlo simulations, Comput. Mater. Sci. **173**, 109363 (2020).

[36] J. Glaser, T. D. Nguyen, J. A. Anderson, P. Lui, F. Spiga, J. A. Millan, D. C. Morse, and S. C. Glotzer, Strong scaling of general-purpose molecular dynamics simulations on GPUs, Comput. Phys. Commun. **192**, 97 (2015).

[37] V. Ramasubramani, B. D. Dice, E. S. Harper, M. P. Spellings, J. A. Anderson, and S. C. Glotzer, Freud: A software suite for high throughput analysis of particle simulation data, Comput. Phys. Commun. **254**, 107275 (2020).

[38] C. S. Adorf, P. M. Dodd, V. Ramasubramani, and S. C. Glotzer, Simple data and workflow management with the signac framework, Comput. Mater. Sci. **146**, 220 (2018).

[39] See Supplemental Material at http://link.aps.org/supplemental/10.1103/PhysRevLett.128.188001 for details of the methodology, how the phase diagram was computed, the order parameters used, and the results of simulations not shown in the main text.

[40] W. G. Hoover, M. Ross, K. W. Johnson, D. Henderson, J. A. Barker, and B. C. Brown, Soft sphere equation of state, J. Chem. Phys. **52**, 4931 (1970).

[41] G. J. Martyna, D. J. Tobias, and M. L. Klein, Constant pressure molecular dynamics algorithms, J. Chem. Phys. **101**, 4177 (1994).

[42] C. Vega and E. G. Noya, Revisiting the Frenkel-Ladd method to compute the free energy of solids: The Einstein molecule approach, J. Chem. Phys. **127**, 1 (2007).

[43] C. L. Phillips, J. A. Anderson, and S. C. Glotzer, Pseudo-random number generation for Brownian Dynamics and Dissipative Particle Dynamics simulations on GPU devices, J. Comput. Phys. **230**, 7191 (2011).

[44] D. Frenkeland and A. J. C. Ladd, New Monte Carlo method to compute the free energy of arbitrary solids. Application to the fcc and hcp phases of hard spheres, J. Chem. Phys. **81**, 3188 (1984).

[45] P. J. Steinhardt, D. R. Nelson, and M. Ronchetti, Bond-orientational order in liquids and glasses, Phys. Rev. B **28**, 784 (1983).

[46] A. Stukowski, Visualization and analysis of atomistic simulation data with OVITO-the Open Visualization Tool, Model. Simul. Mater. Sci. Eng. **18**, 015012 (2010).

[47] J. A. Anderson, M. Eric Irrgang, and S. C. Glotzer, Scalable Metropolis Monte Carlo for simulation of hard shapes, Comput. Phys. Commun. **204**, 21 (2016).

[48] G. C. Sosso, J. Chen, S. J. Cox, M. Fitzner, P. Pedevilla, A. Zen, and A. Michaelides, Crystal nucleation in liquids: Open questions and future challenges in molecular dynamics simulations, Chem. Rev. **116**, 7078 (2016).

[49] P. K. Bommineni, N. R. Varela-Rosales, M. Klement, and M. Engel, Complex Crystals from Size-Disperse Spheres, Phys. Rev. Lett. **122**, 128005 (2019).

[50] C. S. Towler, R. J. Davey, R. W. Lancaster, and C. J. Price, Impact of molecular speciation on crystal nucleation in polymorphic systems: The conundrum of γ glycine and molecular ‘self poisoning’, J. Am. Chem. Soc. **126**, 13347 (2004).

[51] P. Bartlett, A model for the freezing of binary colloidal hard spheres, J. Phys. Condens. Matter **2**, 4979 (1990).

[52] F. A. Escobedo, Effect of inter-species selective interactions on the thermodynamics and nucleation free-energy barriers of a tessellating polyhedral compound, J. Chem. Phys. **145**, 211903 (2016).

[53] T. C. Moore, J. A. Anderson, and S. C. Glotzer, Shape-driven entropic self-assembly of an open, reconfigurable, binary host–guest colloidal crystal, Soft Matter **17**, 2840 (2021).

[54] D. Coslovich, M. Ozawa, and L. Berthier, Local order and crystallization of dense polydisperse hard spheres, J. Phys. Condens. Matter **30**, 144004 (2018).

[55] M. Dijkstra, R. van Roij, and R. Evans, Phase diagram of highly asymmetric binary hard-sphere mixtures, Phys. Rev. E **59**, 5744 (1999).

[56] J. Towns, T. Cockerill, M. Dahan, I. Foster, K. Gaither, A. Grimshaw, V. Hazlewood, S. Lathrop, D. Lifka, G. D. Peterson, R. Roskies, J. R. Scott, and N. Wilkins-Diehr, Xsede: Accelerating scientific discovery, Comput. Sci. Eng. **16**, 62 (2014).

Supplementary Information for Tuning Stoichiometry to Promote Formation of Binary Colloidal Superlattices

R. Allen LaCour,† Timothy C. Moore,† and Sharon C. Glotzer*,†,‡

†*Department of Chemical Engineering, University of Michigan, Ann Arbor, Michigan*

‡*Biointerfaces Institute, University of Michigan, Ann Arbor, Michigan*

E-mail: sglotzer@umich.edu

S1 Simulation Methods

We used molecular dynamics (MD) with the HOOMD-Blue simulation toolkit[1,2] to study the binary inverse power law (IPL) potential with power $n = 50$:

$$U(r_{ij}) = \epsilon\Big(\frac{\sigma_{ij}}{r_{ij}}\Big)^{50}. \tag{1}$$

The quantity U is the potential energy of interaction between two particles i and j at a distance of r_{ij}. The quantity σ_{ij} represents the diameter of the particles; for interactions between unlike particles, we set it to their average diameter. We denote the diameter of the large particles as σ and diameter ratio between small and large particles as γ. The unit of energy is ϵ, which is set to 1 throughout this work. The IPL exhibits thermodynamic scaling between temperature and pressure such that a change in temperature can be mapped to an equivalent change in pressure;[3] thus we only need to investigate its behavior at a single temperature. We truncated the potential at a cutoff of $1.3\sigma_{ij}$ and shifted it from an energy of $2.0{\cdot}10^{-6}\epsilon$ at the cutoff to zero.

We used NPT simulations based on the MTK equations[4] to collect data on nucleation from a fluid and growth from a seed and when computing the intermediate scattering function between large particles ($F_{LL}(q,t)$). Relaxation times (τ_r) were computed by fitting the decay of the first peak in $F_{LL}(q,t)$ to a stretched exponential of the form $a_0 e^{(-t/\tau_r)^\beta}$.

We used HOOMD-Blue's Hard Particle Monte Carlo module to simulate the mixtures of cuboctahedra and octahedra. On-stoichiometry simulations at $N_L{:}N_S = 1{:}1$ consisted of a slow compression from a packing fraction of 0.565 to 0.635 in increments of 0.001. Off-stoichiometry simulations at $N_L{:}N_S = 1{:}2$ consisted of a slow compression from a packing fraction of 0.565 to 0.615 in increments of 0.001. We compressed to a higher packing fraction at $N_L{:}N_S = 1{:}1$ because the system had not finished crystallizing at 0.615, while the system at $N_L{:}N_S = 1{:}2$ was crystalline by that packing fraction.

We used Steinhardt order parameters[5] to classify particles as having AlB_2, mixed FCC-AlB_2, or fluid environments. We discuss our specific use in section S3 of the supplementary material. The freud software library[6] was used to calculate radial distribution functions and Steinhardt order parameters. We used Ovito[7] to visualize particles throughout the work.

The computational workflow was supported by the signac data management framework.[8]

S2 Phase Diagram Calculations

To compute the phase diagram in Figure 1, we needed the specific Gibb's free energy ($\hat{G}$) of every candidate phase. In every case, we first computed a reference free energy for the phase at one pressure (P_{ref}) and then used pressure-volume data to find the free energy $\hat{G}$ any other pressure (P):

$$\hat{G}(P) = \hat{G}(P_{\mathrm{ref}}) + \int_{P_{\mathrm{ref}}}^{P} \hat{V}\, dP \tag{2}$$

where $\hat{V}$ indicates the specific volume.

S2.1 Solid Phases

The reference free energy for the solid was computed from the Einstein molecule method,[9] a variant of the Frenkel-Ladd method[10] in which a single particle is fixed instead of the center of mass. This method returns the specific Helmholtz free energy ($\hat{A}$). Our results are shown in Table S1. The last number in parenthesis was the standard deviation$\cdot 10^3$ obtained from repeating the calculation three times. The temperature (kT) and the de Broglie wavelength were always set to a value of 1 in our calculations. The Langevin integrator[11] within HOOMD-Blue was used when performing the Einstein molecule method.

Table S1: Free energies from Einstein molecule method

Structure	$\rho\sigma^3$	A/kT
FCC_L	1.0179	5.065(1)
AlB_2	2.66	6.897(6)
NaZn_{13}	4.803	6.700(3)
FCC_S	6.1181	6.860(1)

We did not perform separate Einstein molecule calculations for FCC_S. Instead, we used the fact that the thermodynamics of FCC_L and FCC_S are identical at $\rho\sigma^3_{LL} = \rho\sigma^3_{SS}$ except for the less volume overall in FCC_S. This leads to the following relation being exact:

$$\hat{A}_{\mathrm{FCC_S}}\left(\rho\left(\frac{\sigma}{0.55}\right)^3\right) = \hat{A}_{\mathrm{FCC_L}} - 3kT\ln 0.55 \tag{3}$$

We also estimated our accuracy in a second way. Specifically, we estimated the free energy at another density using thermodynamic integration (using the PV data shown below) and using the reference values given in Table S1. We then compared this to performing a new Einstein molecule calculation at the other density. Our results are shown in Table S2.

From these calculations we feel confident that our errors are low ($< 0.01kT$) in the Einstein Molecule and thermodynamic integration calculations.

Table S2: Comparison between Enstein molecule method and PV integration.

Structure	$\rho\sigma^3$	$\hat{A}_{int}/kT$	$\hat{A}_{ein}/kT$	$\Delta\hat{A}/kT$
FCC_L	1.35	12.546	12.538	0.008
AlB_2	3.371	16.946	16.940	0.006
$NaZn_{13}$	6.105	13.113	13.111	0.002
FCC_S	8.1142	14.340	14.332	0.008

For the solid phases, we fit PV data collected in simulations to the following form:

$$\rho = \frac{\sum\limits_{n=0} a_n P^n}{1 + b_1 P} \tag{4}$$

where a_n and b_1 are coefficients specific to each crystal. Their values are given in Table S3. No equation of state was constructed for FCC_S because its free energy could be computed using equation 4 in conjunction with the equation of state for FCC_L.

Table S3: Coefficients for Solid equation of States

Coefficient	FCC_L	AlB_2	$NaZn_{13}$
a_0	-1.6285	$-2.6111 \cdot 10^{-1}$	$-2.1729 \cdot 10^{1}$
a_1	1.0422	$8.0842 \cdot 10^{-1}$	2.5387
a_2	$2.6596 \cdot 10^{-3}$	$5.4927 \cdot 10^{-4}$	$1.9206 \cdot 10^{-3}$
a_3	$-2.9744 \cdot 10^{-5}$	$-1.6527 \cdot 10^{-6}$	$-6.3093 \cdot 10^{-6}$
a_4	$2.4106 \cdot 10^{-7}$	$3.7277 \cdot 10^{-9}$	$1.5602 \cdot 10^{-8}$
a_5	$-1.1000 \cdot 10^{-9}$	$-4.8345 \cdot 10^{-12}$	$-2.2451 \cdot 10^{-11}$
a_6	$2.0939 \cdot 10^{-12}$	$2.6248 \cdot 10^{-15}$	$1.3806 \cdot 10^{-14}$
b_1	$8.3461 \cdot 10^{-1}$	$2.6407 \cdot 10^{-1}$	$4.5643 \cdot 10^{-1}$

We note that the perfect (without defects) solid phases must coexist with another phase at any stoichiometry other than that of the perfect crystal. However, compositional disorder may cause them to be the only thermodynamically stable phase for stoichiometries representing a slight excess of large or small particles. We do not consider such compositional disorder here because it is difficult to quantify with standard free energy calculations and because we think it will negligibly affect equilibrium phase behavior. With regards to the second point, the large size differences between the particles makes substitutional defects unfavorable and even a large excess of one component will only change the stoichiometry of the solid slightly. For example, a large excess of 10% small particles would only lead $\mathrm{AlB_2}$'s N_L:N_S to change from 1:2 to 1:2.2 and for its x_s to change from $0.\overline{666}$ to 0.6875. We also note that this assumption is consistent with previous work.[12–14]

S2.2 Fluid Phases

The reference state for the fluid was a low density fluid, for which the free energy could be calculated using the first few virial coefficients. We used just the second (B_2) and third virial (B_2) coeficients:

$$A_{ref,Fluid} = kT(\ln \rho\Lambda^3 - 1 + B_2\rho + B_3\rho^2/2 + x_s \ln x_s + x_L \ln x_L) \tag{5}$$

where x_L and x_S are the fraction of large and small particles, respectively. We again set the de Broglie wavelength (Λ) to 1. For the IPL, the second virial coefficient is given by:

$$B_2 = 2.174826\left(x_L^2 + 2\left(\frac{1+0.55}{2}\right)^3 x_L x_s + 0.55^3 x_s^2\right) \tag{6}$$

The third virial coefficient is given by:

$$B_3 = 2.947x_L^3 + 3\cdot 0.998x_L^2 x_S + 3\cdot 0.298x_L x_S^2 + 0.0816x_S^3 \tag{7}$$

We did not use the fourth virial coeffiecient in our calculation of $A_{ref,Fluid}$, but we do in our equation of state. It is given by:

$$B_4 = 2.909x_L^4 + 4\cdot 0.8378x_L^3 x_S + 6\cdot 0.274x_L^2 x_S^2 + 4\cdot 0.0560x_L x_S^3 + 0.0134x_s^4 \tag{8}$$

B_2 was calculated with the standard expression; B_3 and B_4 were calculated using importance sampling.

We also constructed an equation of state for the liquid:

$$P\lambda/kT = d + B_2 d^2/\lambda + B_3 d^3/\lambda^2 + B_4 d^4/\lambda^3 + v_5 y_5 d^5 + v_6 y_6 d^5 + v_7 y_7 d^7 \tag{9}$$

The quantity λ is given by:

$$\lambda = x_L + 0.55^3 x_S \tag{10}$$

The term d is a transformation of density:

$$d = \rho\lambda \tag{11}$$

The v_i terms are further density transformations:

$$v_i = v_{i,0} + v_{i,1} d + v_{i,2} d^2 + v_{i,3} d^3 \tag{12}$$

The y_i terms are transformations of the stoichiometry:

$$y_i = 1 + y_{i,1} x_L * x_S + y_{i,2} x_L * x_S^2 + y_{i,3} x_L * x_S^3 + y_{i,4} x_L * x_S^4 + y_{i,5} x_L x_S^5 \tag{13}$$

The coefficients for v_i and y_i are given below:

Table S4: Fluid equation of state v_i

Coefficient	$i = 5$	$i = 6$	$i = 7$
$v_{i,0}$	1.74004391	14.19132885	-324.4696625
$v_{i,1}$	15.71505006	-85.21851339	532.64233085
$v_{i,2}$	-77.66842443	63.29969841	-361.40158691
$v_{i,3}$	154.19500341	-18.72471099	93.13536666

We did not fit for $y_{6,5}$ and $y_{7,5}$, so we fit 25 parameters in total (all of the v_i and y_i). To perform the fitting we collected data for the pressure at 543 combinations of ρ and x_s.

Table S5: Fluid equation of state y_i

Coefficient	$i = 5$	$i = 6$	$i = 7$
$y_{i,1}$	-0.23302827	-12.13353876	5.01938459
$y_{i,2}$	-1.17507739	36.90126947	-18.09714247
$y_{i,3}$	1.82466147	-31.03854651	16.95036767
$y_{i,4}$	-2.17097489	-0.19534053	-4.0778357
$y_{i,5}$	-0.39585797	1	1

S2.3 Phase Diagram

In our phase diagram in Figure 1, we show the phase or combination of phases coexisting together that minimizes G at different x_S and P^*. We did this by making a grid of different x_s and P^*, computing the free energy of possible combinations of phases at that point, and looking for the combination that minimized free energy. We used a resolution of 0.25 P^* and 0.0025 x_s in our grid.

Because we do not consider compositional disorder, evaluating the free energy of a pair of coexisting solid phases was simple:

$$\hat{G}(P^*, x_S) = (1 - x_{C2}(x_S))\hat{G}_{C1}(P^*) + x_{C2}(x_S)\hat{G}_{C2}(P^*) \tag{14}$$

where x_{C2} is the fraction of particles in second solid phase and $\hat{G}_{C1}$ and $\hat{G}_{C2}$ are the free energies of the two solid phases. The quantity x_{C2} can determined from x_S using the lever rule and the stoichiometry of the solids.

The common tangent method can be used to find the composition of a fluid phase in equilibrium with a solid phase. Typically, one looks for the common tangent curve of the dips in the curve of $\hat{G}$ vs. x_S, where each dip corresponds to a particular phase. If one phase is confined to one stoichiometry (*e.g.*, FCC$_L$ at $x_S = 0$ and AlB$_2$ at $x_S = 2/3$), the tangent curve needs to intersect the x_S and $\hat{G}$ of that phase. We illustrate this process that in Figure S1.

This process for find the common tangent is equivalent to finding the fluid x_S where the

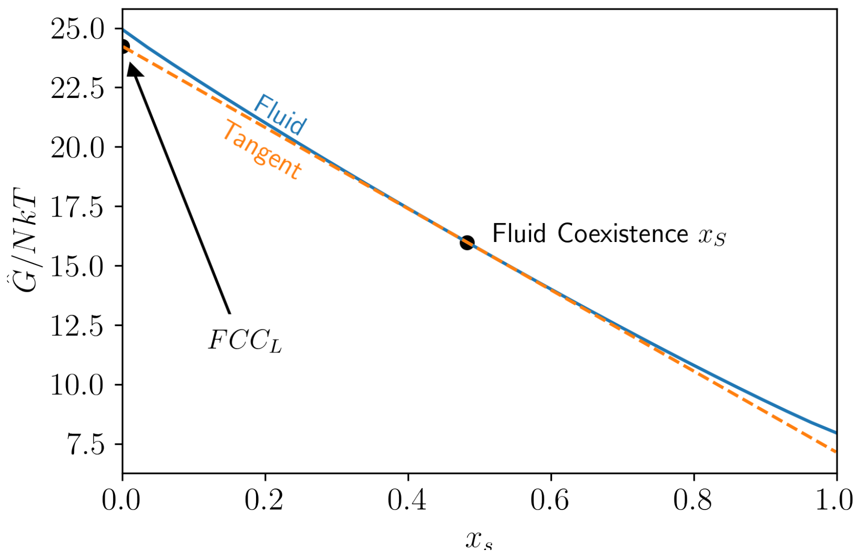

Figure S1: Illustration of computing FCC_L-fluid coexistence points. The fluid G/NkT is given in blue and labelled “Fluid”. The x_s of the fluid in coexistence with FCC$_L$ is given by finding the tangent line that intersects the point indicating FCC_L's G/NkT. The results shown are for $P^* = 20$.

following equation holds:

$$\hat{G}_C = (1 - x_C)\mu_F^L + x_C\mu_F^S \tag{15}$$

where quantity $\hat{G}_C$ is the chemical potential of the crystal; x_C is the fraction of small particles in the crystal; and μ_F^L and μ_F^S are the chemical potentials of the large and small species in the fluid, respectively. The chemical potential of each species can be found by computing where the tangent curve intersects $x_S = 0$ and $x_S = 1$. These points are also indicated in Figure S1.

S3 Order parameter

We use Steinhardt order parameters to classify particles according to their coordination environment. We show in Figure S2 that a combination of two order parameters can distinguish whether large particles are in fluid, AlB$_2$ (Figure S2a), or “mixed FCC-AlB$_2$” (Figure S2b) environments, which we show to be a common defect during AlB$_2$ self-assembly. The black lines in Figure S2c show how we classify particles with specific q_6^{LL} and $q_8^{LL,LS}$ into the three environments. For the mixed FCC-AlB$_2$ environments, we simulated a structure involving alternating layers of a hexagonally close packed crystal and AlB$_2$ crystals and computed the order of the particles at the interface; a visualization of the structure is shown in Figure S3. We note that our order parameter will somewhat underestimate the number of crystalline particles because it does not detect particles at the edges of crystal grains. We computed that our order parameter misclassified particles in the fluid with a rate under 0.25%.

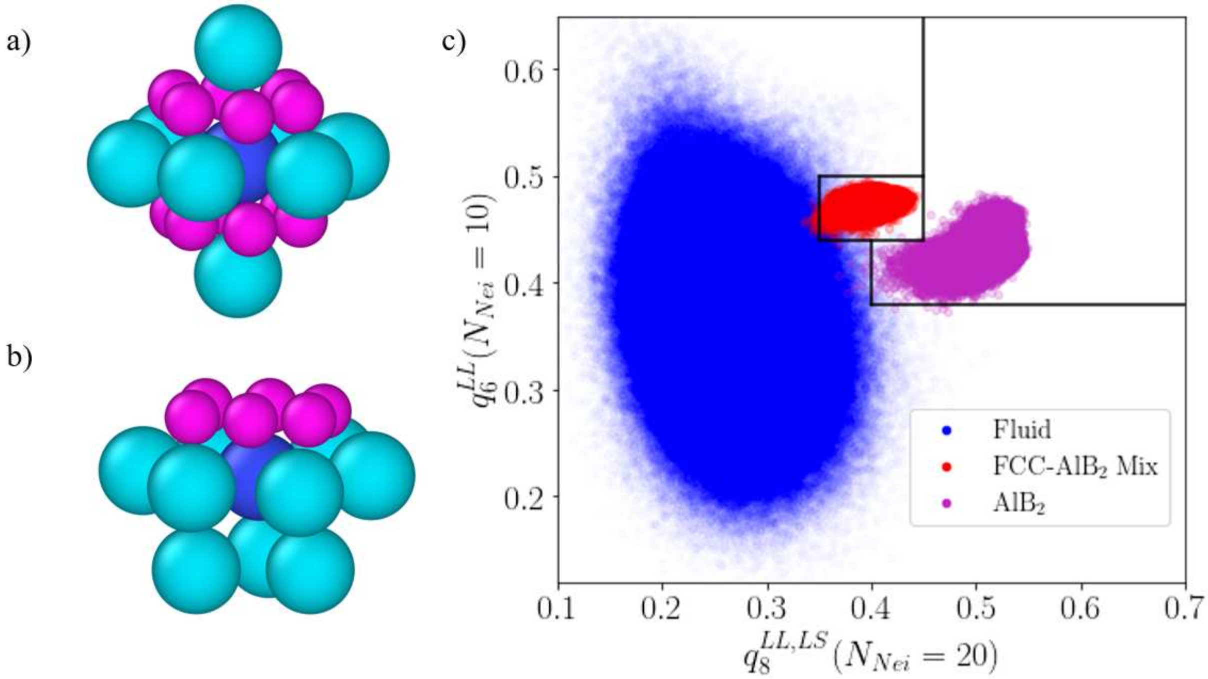

Figure S2: The coordination of large particles in a) AlB$_2$ and b) mixed FCC-AlB$_2$ environments; c) the Steinhardt order parameters of large particles in those environments and a fluid environment at N_L:N_S = 1:2. In a) and b) the reference particle is colored dark blue We use the Steinhardt order parameter q_8 for the first 20 neighbors (the number of neighbors of each large particle in the perfect AlB$_2$ crystal) of either type, and the q_6 for the first 10 *large* neighbors. The data for AlB$_2$ and mixed FCC-AlB$_2$ were generated from simulations of pre-assembled versions of the structures. The structure used for mixed FCC-AlB$_2$ is shown in Figure S4. The black lines in c correspond to how we classified particles. The distribution of order parameters shown in c) is computed at $P^* = 60$.

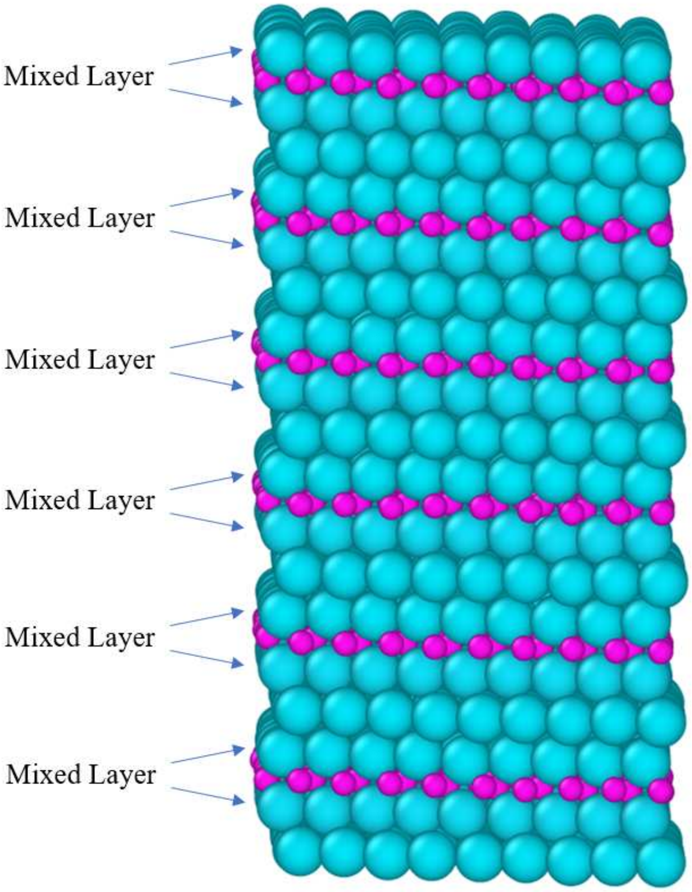

Figure S3: Snapshot of the structure we used to determine the order parameter for “mixed FCC-AlB_2” environments. We only computed the order parameter for layers denote ”Mixed Layer”.

S4 Different Stoichoimetries and RDFs

We present RDFs and snapshots for our results at each stoichiometry in Figures S4-6.

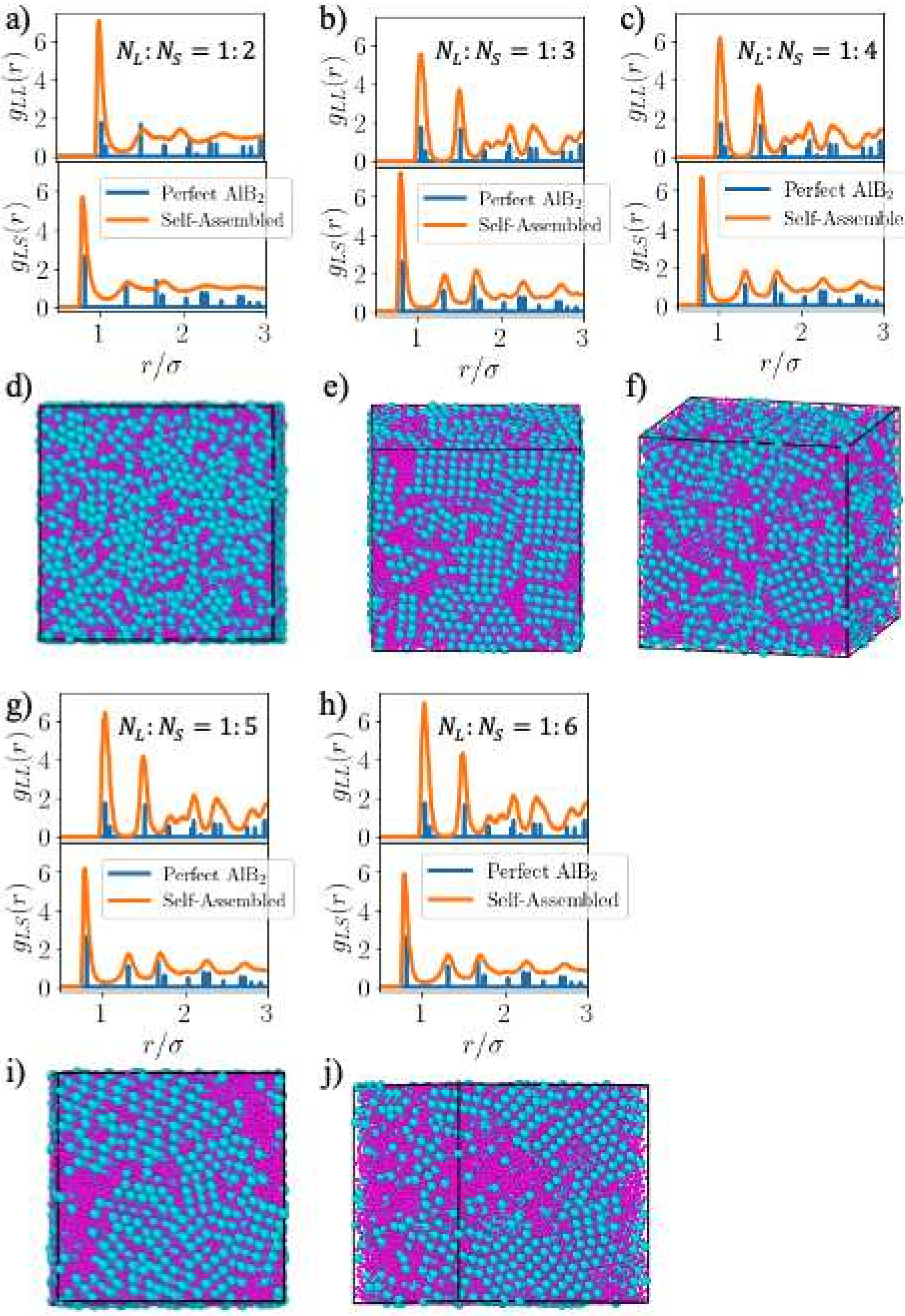

Figure S4: Radial distribution functions (RDFs) and and snapshots of NPT simulation results at (a,d) N_L:N_S = 1:2, $P^* = 70$, (b,e) N_L:N_S = 1:3, $P^* = 70$, (c,f) N_L:N_S = 1:4, $P^* = 78$, (g,i) N_L:N_S = 1:5, $P^* = 75$, and (h,j) N_L:N_S = 1:6, $P^* = 80$. These simulations all began in a fluid-state. The RDFs are averaged over the final 5 frames of the simulations; the snapshots are the last frames of the simulations. We only show the RDFs for large-large and large-small interactions because that of small-small interactions tends to be dominated by fluid-like small particles. At both stoichiometries, we see crystal grains in both the snapshots and the RDFs. Visual inspection and comparing the RDFs to the perfect ones for AlB$_2$ show the crystal structure to be that of AlB$_2$.

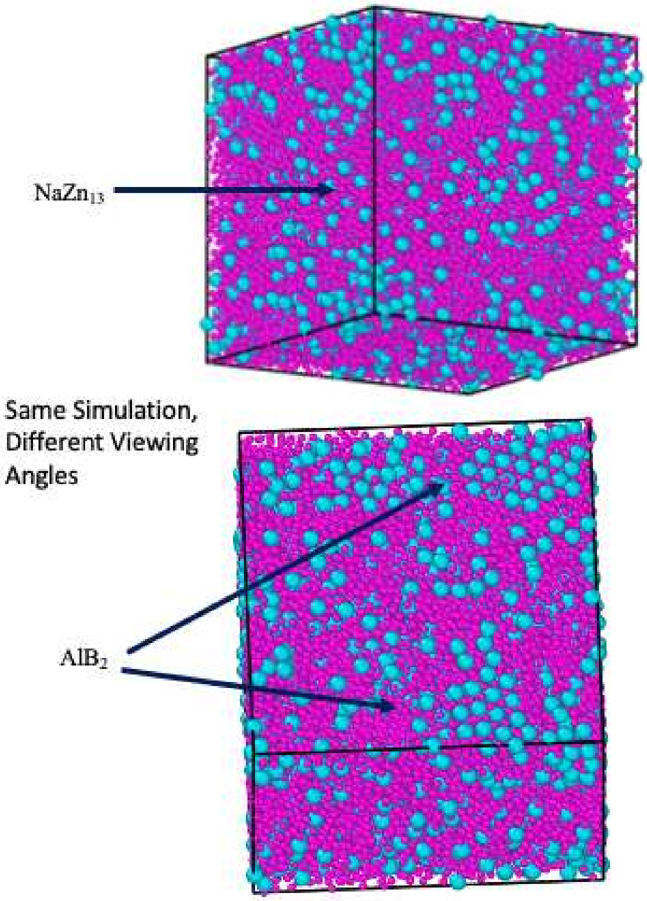

Figure S5: Snapshots showing different angles of an NPT simulation run at N_L:N_S = 1:9 and $P^* = 98$. The simulation began in a fluid-state. Both AlB_2 and $NaZn_{13}$ self-assemble in the simulation, as point out by the arrows. The crystal grains are small in both cases.

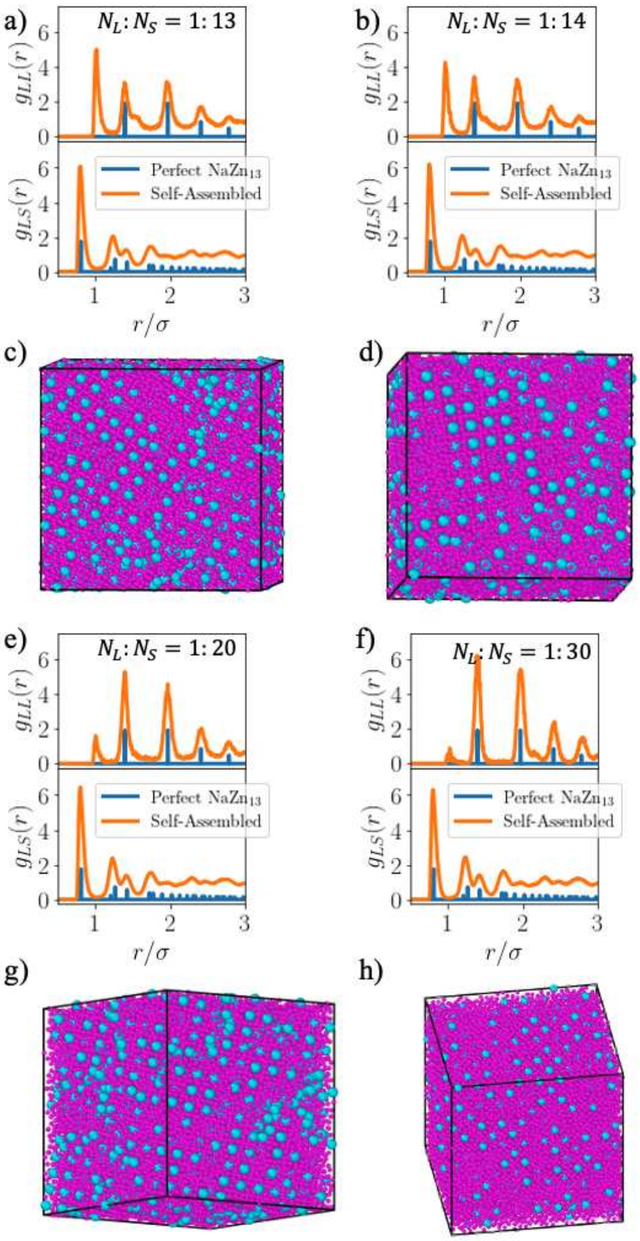

Figure S6: Radial distribution functions (RDFs) and and snapshots of NPT simulation results at (a,c) N_L:N_S = 1:13, $P^* = 98$, (b,d) N_L:N_S = 1:14, $P^* = 98$, (e,g) N_L:N_S = 1:20, $P^* = 98$, and (f,h) N_L:N_S = 1:30, $P^* = 98$. These simulations all began in a fluid-state. The RDFs are averaged over the final 5 frames of the simulations; the snapshots are the last frames of the simulations. We only show the RDFs for large-large and large-small interactions because that of small-small interactions tends to be dominated by fluid-like small particles. At both stoichiometries, we see crystal grains in both the snapshots and the RDFs. Visual inspection and comparing the RDFs to the perfect ones for NaZn$_1$3 show the crystal structure to be that of NaZn$_1$3. We note presence of an unexpected peak at $r/\sigma = 1$; this is due to large particles in contact with each. There are no such contacts in perfect NaZn$_1$3, but they occur in our self-assembly due to some large particles not being incorporated into the crystal.

References

1. Anderson, J. A.; Lorenz, C. D.; Travesset, A. General purpose molecular dynamics simulations fully implemented on graphics processing units. *J. Comput. Phys.* **2008**, *227*, 5342–5359.

2. Glaser, J.; Nguyen, T. D.; Anderson, J. A.; Lui, P.; Spiga, F.; Millan, J. A.; Morse, D. C.; Glotzer, S. C. Strong scaling of general-purpose molecular dynamics simulations on GPUs. *Comput. Phys. Commun.* **2015**, *192*, 97–107.

3. Hoover, W. G.; Ross, M.; Johnson, K. W.; Henderson, D.; Barker, J. A.; Brown, B. C. Soft Sphere Equation of State. *J. Chem. Phys.* **1970**, *52*, 4931–4941.

4. Martyna, G. J.; Tobias, D. J.; Klein, M. L. Constant pressure molecular dynamics algorithms. *J. Chem. Phys.* **1994**, *101*, 4177–4189.

5. Steinhardt, P. J.; Nelson, D. R.; Ronchetti, M. Bond-orientational order in liquids and glasses. *Phys. Rev. B* **1983**, *28*, 784–805.

6. Ramasubramani, V.; Dice, B. D.; Harper, E. S.; Spellings, M. P.; Anderson, J. A.; Glotzer, S. C. freud: A software suite for high throughput analysis of particle simulation data. *Comput. Phys. Commun.* **2020**, *254*, 107275.

7. Stukowski, A. Visualization and analysis of atomistic simulation data with OVITO–the Open Visualization Tool. *Model. Simul. Mater. Sci. Eng* **2010**, *18*, 015012.

8. Adorf, C. S.; Dodd, P. M.; Ramasubramani, V.; Glotzer, S. C. Simple data and workflow management with the signac framework. *Comput. Mater. Sci.* **2018**, *146*, 220–229.

9. Vega, C.; Noya, E. G. Revisiting the Frenkel-Ladd method to compute the free energy of solids: The Einstein molecule approach. *J. Chem. Phys.* **2007**, *127*, 1–12.

10. Frenkel, D.; Ladd, A. J. C. New Monte Carlo method to compute the free energy of arbitrary solids. Application to the fcc and hcp phases of hard spheres. *J. Chem. Phys.* **1984**, *81*, 3188–3193.

11. Phillips, C. L.; Anderson, J. A.; Glotzer, S. C. Pseudo-random number generation for Brownian Dynamics and Dissipative Particle Dynamics simulations on GPU devices. *J. Comput. Phys.* **2011**, *230*, 7191–7201.

12. Eldridge, M. D.; Madden, P. A.; Frenkel, D. Entropy-driven formation of a superlattice in a hard-sphere binary mixture. *Nature* **1993**, *365*, 35–37.

13. Hynninen, A. P.; Thijssen, J. H.; Vermolen, E. C.; Dijkstra, M.; Van Blaaderen, A. Self-assembly route for photonic crystals with a bandgap in the visible region. *Nat. Mater.* **2007**, *6*, 202–205.

14. Escobedo, F. A. Effect of inter-species selective interactions on the thermodynamics and nucleation free-energy barriers of a tessellating polyhedral compound. *J. Chem. Phys.* **2016**, *145*, 211903.